Micro- and Nanostructure Analysis of Vapor-Phase-Grown AlN on Face-to-Face Annealed Sputtered AlN/Nanopatterned Sapphire Substrate Templates

Yudai Nakanishi[1] · Yusuke Hayashi[1] · Takeaki Hamachi[1] · Tetsuya Tohei[1] · Yoshikata Nakajima[2] · Shiyu Xiao[3] · Kanako Shojiki[3,4] · Hideto Miyake[3] · Akira Sakai[1]

Abstract

Micro- and nanostructures in vapor-phase-grown AlN on face-to-face annealed sputtered AlN (FFA Sp-AlN) templates formed on nanopatterned sapphire substrates (NPSS) were comprehensively analyzed using transmission electron microscopy. The comparison between metal–organic vapor-phase epitaxy-grown AlN/FFA Sp-AlN/hole-type NPSS (Sample MOH) and hydride vapor-phase epitaxy-grown AlN/FFA Sp-AlN/cone-type NPSS (Sample HVC) showed apparent differences in the morphology of dislocation propagation, presence of voids, shape of polarity inversion boundaries, and crystal structure on the slope region of NPSS. Notably, cross-sectional and plan-view observations revealed that the quality of FFA Sp-AlN significantly affects the threading dislocation density in the vapor-phase-grown layer. At the slope region of the AlN/NPSS interface, γ-AlON was observed in the MOH sample, while highly misaligned AlN grains were observed in the HVC sample. These characteristic crystal structures affect the occurrence of dislocations via different mechanisms in each sample. This study provides practical information for strategically controlling the micro- and nanostructures formed in AlN/NPSS structures for high-performance AlGaN-based deep-ultraviolet emitters.

✉ Yudai Nakanishi
  u714116a@ecs.osaka-u.ac.jp

✉ Yusuke Hayashi
  hayashi@ee.es.osaka-u.ac.jp

✉ Akira Sakai
  sakai@ee.es.osaka-u.ac.jp

1 Graduate School of Engineering Science, Osaka University, 1-3 Machikaneyama-cho, Toyonaka, Osaka 560-8531, Japan

2 R3 Institute for Newly-Emerging Science Design, Osaka University, 1-3 Machikaneyama-cho, Toyonaka, Osaka 560-8531, Japan

3 Graduate School of Engineering, Mie University, 1577 Kurimamachiya-cho, Tsu, Mie 514-8507, Japan

4 Graduate School of Engineering, Osaka University, 2-1 Yamadaoka, Suita, Osaka 565-0871, Japan

Introduction

AlN grown on sapphire substrates is transparent to deep-ultraviolet (DUV) light, less expensive than AlN freestanding substrates, and used as the substrate part of DUV light-emitting diodes (LEDs) and laser diodes.[1–10] DUV light has several applications in sterilization, water purification, sensing, and biochemical industries.[11–13] The recent global outbreak of COVID-19 has increased the demand for DUV light with the ability to inactivate severe acute respiratory syndrome coronavirus.[14–16] The realization of high-quality AlN templates is essential for developing high-performance DUV light emitters.

Miyake et al. reported a method for fabricating inexpensive and high-quality AlN layers on sapphire substrates by combining the sputtering method with annealing in a face-to-face setup (FFA Sp-AlN).[17] The AlN template fabricated by this method achieved a record-low threading dislocation density in the 10^7 cm^{-2} range and has attracted attention for its application in AlGaN-based DUV LEDs.[18,19]

Consequently, DUV LEDs fabricated on FFA Sp-AlN achieved an external quantum efficiency (EQE) of 8.0% at 263 nm, a wavelength with a high bactericidal effect.[20] An attempt to fabricate FFA Sp-AlN templates in combination with nanopatterned sapphire substrates (NPSS) has also been reported.[21,22] Since NPSS can prevent cracks by strain relaxation and improve the light extraction efficiency,[22–26] improved EQE is expected when NPSS are implemented in AlGaN DUV LEDs using FFA Sp-AlN. However, the current threading dislocation density of the vapor-phase-grown thick AlN on the FFA Sp-AlN/NPSS template is in the 10^8 cm^{-2} range.[21,22] This threading dislocation density leaves room for improvement compared with the conventional FFA Sp-AlN on flat sapphire and other AlN/NPSS templates fabricated by metal–organic vapor-phase epitaxy (MOVPE).[27–29] To solve this problem, a comprehensive analysis investigating micro- and nanostructures caused by NPSS is required, including the morphology of dislocation

propagation, presence of voids, shape of polarity inversion boundaries, and crystal structure in the slope region of NPSS, which have not yet been elucidated in detail. This study used cross-sectional and plan-view transmission electron microscopy (TEM) to elucidate the unique structures of vapor-phase-grown AlN/FFA Sp-AlN/NPSS and provide a practical solution for dislocation reduction.

Experimental

Two sample types were used in this study. Figure 1a and d show the schematics of the sample structures showing MOVPE-grown AlN on an FFA Sp-AlN/hole-type (HT) NPSS (Sample MOH) and HVPE-grown AlN on an FFA Sp-AlN/cone-type (CT) NPSS (Sample HVC), respectively. In previous studies, four types of samples were prepared by combining two types of NPSS (hole- and cone-type) and
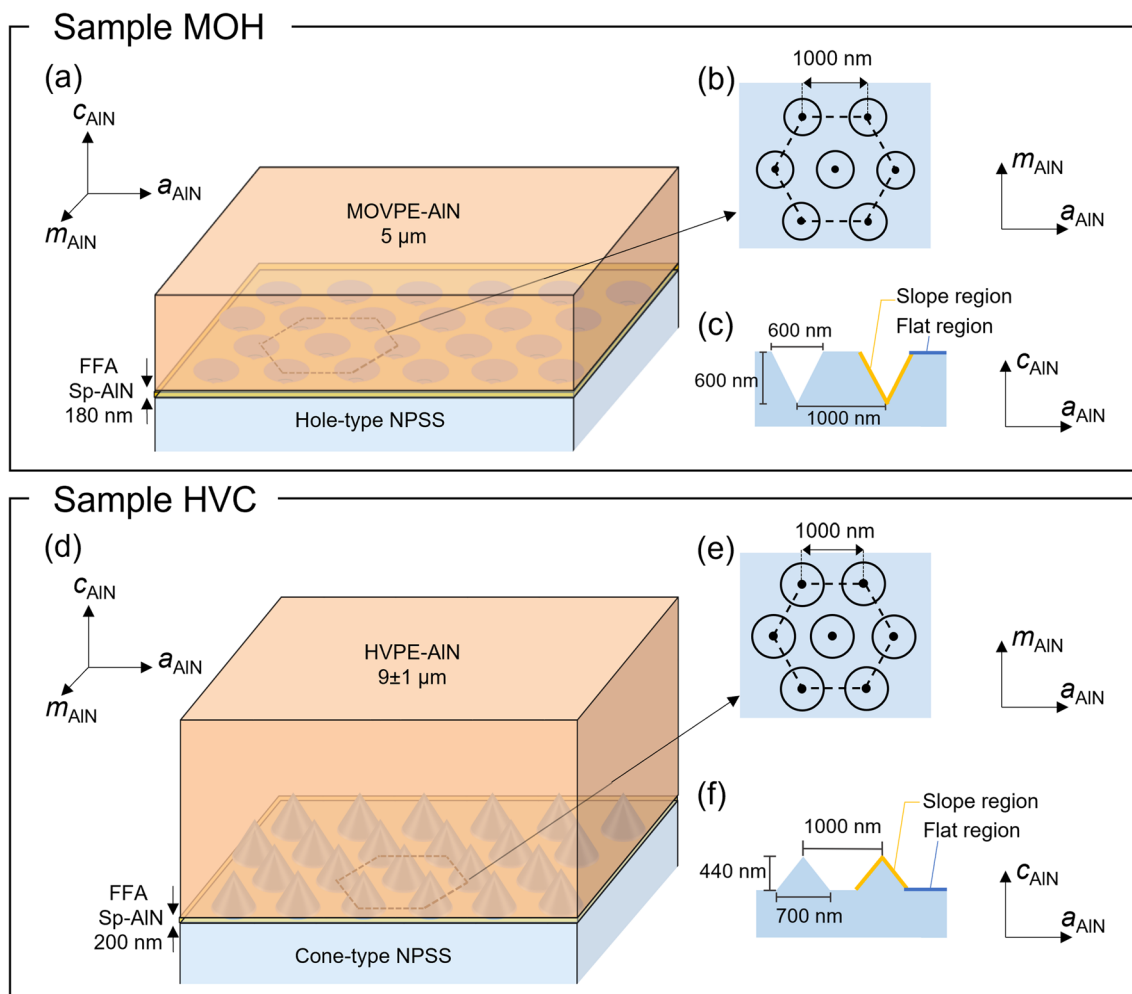
Fig. 1 Schematics of (a) Sample MOH, (b) plan-view geometry of HT-NPSS, (c) cross section of HT-NPSS, (d) Sample HVC, (e) plan-view geometry of CT-NPSS, and (f) cross section of CT-NPSS.

two types of vapor-phase growth methods (MOVPE and HVPE).[21,22] Since relatively high-quality AlN was achieved in Samples MOH and HVC, this study focuses on these two samples to gain knowledge toward further improvement in the crystal quality. A fully comprehensive analysis of the samples prepared by MOVPE growth on CT-NPSS (i.e., MOC) and HVPE growth on HT-NPSS (i.e., HVH) is left for future work. As shown in Fig. 1b and c, the pattern period of HT-NPSS is 1000 nm, and the hole diameter and depth are 600 nm each. Moreover, as shown in Fig. 1e and f, the pattern period, cone diameter, and height of the CT-NPSS were 1000 nm, 700 nm, and 440 nm, respectively. The structural design of the NPSS was based the reports from Zhang et al. for HT-NPSS (period/diameter/depth = 1000 nm/650 nm/2 20 nm)[27] and Fujikura et al. for CT-NPSS (period/diameter/height = 1000 nm/700 nm/440 nm).[30] Zhang et al. revealed that the diameter was a dominant parameter influencing the crystallinity in MOVPE-grown AlN on CT-NPSS since the optimized diameter of 650 nm among 300 nm to 800 nm significantly promoted the bending of the threading dislocations via the image force effect. On the other hand, Fujikura et al. clarified that cone size reduction with a height of less than 440 nm is beneficial to diminish the misoriented HVPE-grown AlN on the slope region of NPSS. Both types of NPSS with a c-plane orientation had an cutoff angle of $0.2°$ to the m-axis direction. The surfaces of both NPSS

consist of flat and slope regions with different configurations, as shown in Fig. 1c and f. We used commercial NPSS which were fabricated using nano-imprint lithography and etching technique.[27] First, 180-nm-thick FFA Sp-AlN and 5-µm-thick MOVPE AlN were formed in Sample MOH, while 200-nm thick FFA Sp-AlN and 9 ± 1-µm-thick HVPE AlN were formed in Sample HVC. FFA was performed for 3 h in a nitrogen atmosphere at 1700°C for both samples. The MOVPE growth of Sample MOH was performed at 1300°C, whereas the HVPE growth of Sample HVC was performed at 1550°C. The detailed fabrication procedure has been described elsewhere.[21,22]

TEM specimens for cross-sectional and plan-view observations were prepared using an FEI Versa 3D™ Dual-Beam™ focused ion beam (FIB) system. These specimens were analyzed using a JEOL JEM-2100 and FEI Tecnai 20 by bright- and dark-field (BF, DF) TEM observations combined with selected area electron diffraction (SAD) and energy-dispersive x-ray spectroscopy (EDS).

Results and Discussion

Figure 2 shows the cross-sectional BF-TEM images of the MOH and HVC samples. Both samples show an arrow-shaped micro-sized void structure (hereafter called
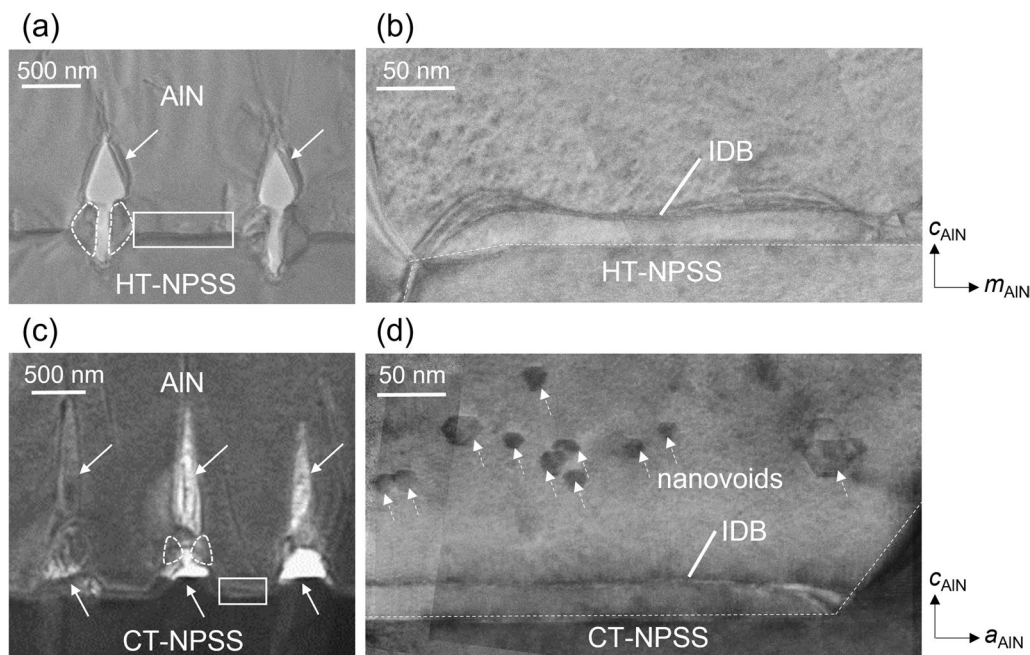
Fig. 2 (a) Cross-sectional TEM image of Sample MOH taken along the AlN $<11\bar{2}0>$ zone axis. (b) Magnified image of the rectangle area in (a). (c) Cross-sectional TEM image of Sample HVC taken along the AlN $<1\bar{1}00>$ zone axis. (d) Magnified image of the rectangle area in (c). In (a) and (c), the white solid arrows and dotted framed areas indicate microvoids and grains on the slope region, respectively. As shown in (b) and (d), a waved inversion domain boundary (IDB) was observed in Sample MOH, while a flat IDB and numerous nanovoids (indicated by white dotted arrows) were observed in Sample HVC.

"microvoid") and the surrounding small grains, which are characteristic of AlN/NPSS, as observed in previous studies.[21,22,29] As indicated by the white arrows in Fig. 2, microvoids exist directly above the NPSS cones or holes, and crystalline domains are observed, as highlighted by the dotted lines. These microvoids with crystalline domains result from the faster growth rates of vapor-phase epitaxy of the flat region than those of the slope regions.[31]

Figure 2b and d are magnified images of the white rectangular regions in Fig. 2a and c, respectively, focusing on the flat region of the NPSS. Sample MOH shows wavy dark contrast lines, indicating an inversion domain boundary (IDB) (see Figs. S1 and S2 of the Supplementary Information for IDB specification by the breakdown of Friedel's law[32–35]). In contrast, Sample HVC shows a linear IDB with randomly distributed hexagonal nano-sized voids (called "nanovoids"). It has been reported that similar linear IDBs and nanovoids were also formed in FFA Sp-AlN on a conventional flat sapphire substrate,[36] and neither the flat IDBs nor the nanovoids degraded the AlN film quality.[37] However, the wavy and columnar IDBs in Sample MOH (see Fig. S3), which have not been observed in the conventional FFA Sp-AlN, are supposed to induce inferior quality to the flat region and the AlN film grown on that region, compared to those in Sample HVC. The IDB in FFA Sp-AlN is possibly thin aluminum oxynitride or aluminum oxide formed via the oxygen incorporation from the AlN sputtering target and sapphire substrate.[36,38,39] Interestingly, universal IDB structures have been observed among FFA Sp-AlN, MOVPE-grown AlN, and molecular beam epitaxy-grown AlN on FFA Sp-AlN.[36–40] Hence, the marked difference in the IDB morphology between Samples MOH and HVC suggests that the type of NPSS modifies how oxygen is supplied from the sapphire and incorporated in FFA Sp-AlN.

Figure 3a and b show the plan-view BF TEM images taken with $g = 11\bar{2}0$ for the regions 200–300 nm above the AlN/NPSS interfaces in the MOH and HVC samples, respectively. The white dashed circles indicate the locations of the NPSS cones and holes. Depending on the shape, dark-contrast dislocations are categorized into two groups: dot-like threading dislocations (red boxes) and line-like basal plane dislocations (yellow arrows). The threading dislocation density (TDD) is measured to be 8.3×10^8 cm^{-2} and 4.7×10^8 cm^{-2} for the MOH and HVC samples, respectively. The distribution of threading dislocations in the red boxes is observed to constitute small-angle grain boundaries,[41] which is likely attributed to the accumulation of dislocations at the boundaries of the slope regions and crystal domains during the solid-phase reaction in FFA.[17] Meanwhile, only a few threading dislocations and no basal-plane dislocations are observed in the HVC sample, indicating a higher crystallinity than that of the MOH sample (see Fig. S4 for a more highlighted contrast of the basal plane dislocations observed by annular DF scanning TEM). The observed remarkable difference in the defect distribution between the two samples probably originates from the crystal quality of the flat region and the crystalline domain structure in the slope region (dotted framed areas in Fig. 2a and c).

We analyzed their crystal structures to investigate the effect of domains in the slope region on the crystal quality in more detail. Figure 4a and c show the cross-sectional and plan-view BF TEM images of Sample MOH taken along the AlN <11$\bar{2}$0> and <0001> zone axes. These two figures show two symmetric domains on either side of the microvoid and
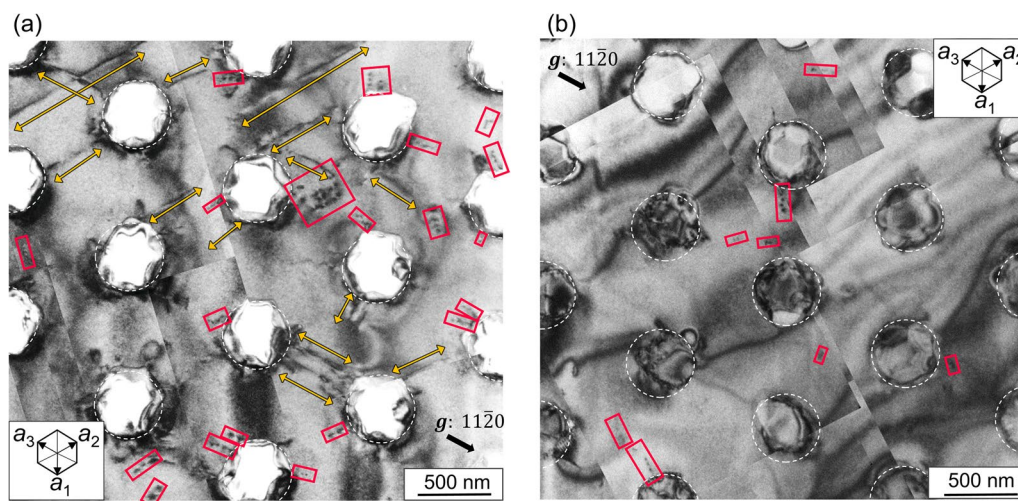
Fig. 3 Plan-view bright-field TEM images of Samples (a) MOH and (b) HVC under a two-beam condition with $g = 11\bar{2}0$. In (a) and (b), the red rectangles and orange arrows indicate arrayed dislocations and basal dislocations, respectively, and the dashed yellow circles indicate the locations of the NPSS pattern.
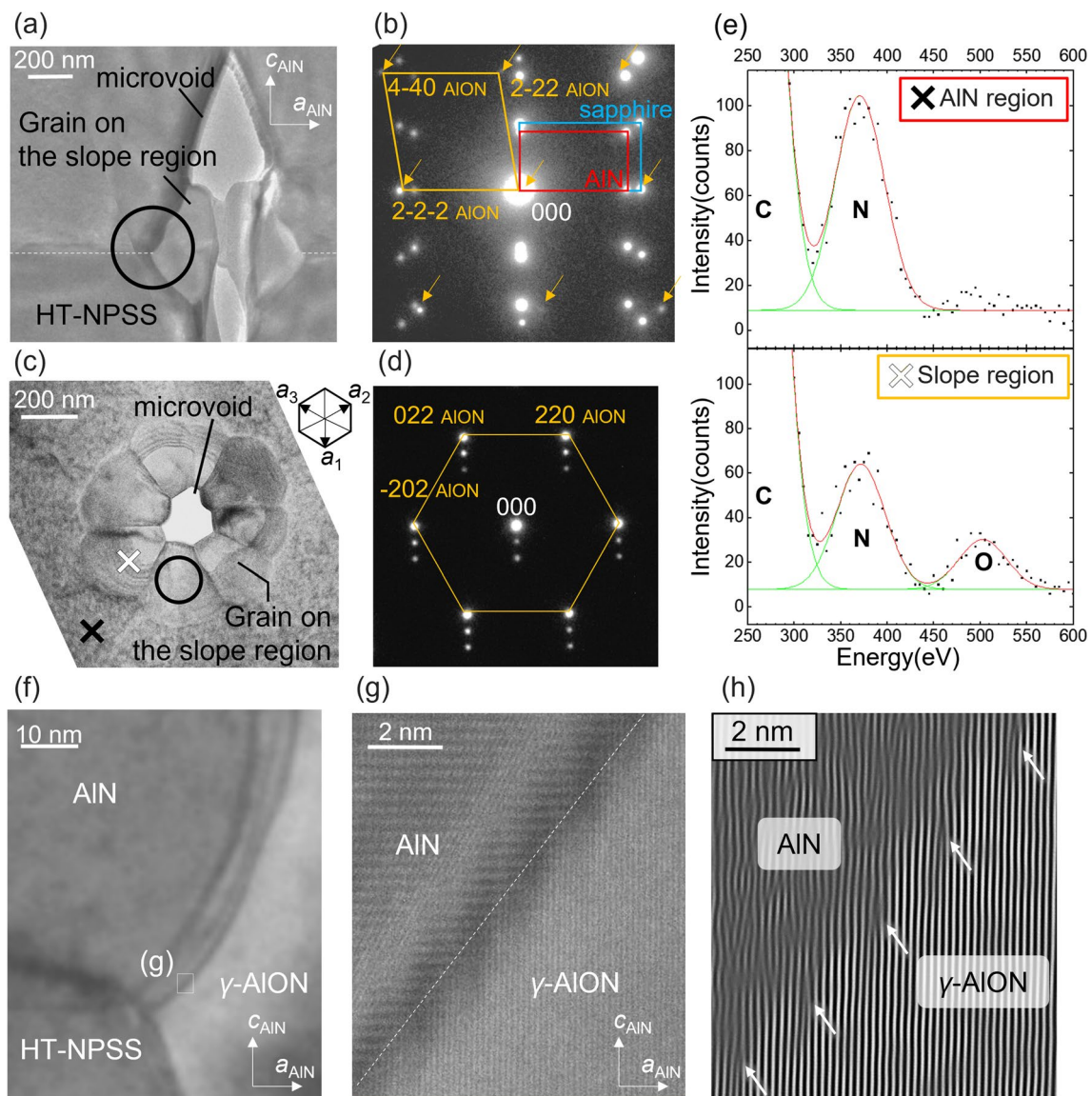
Fig. 4 (a) Cross-sectional TEM image of Sample MOH taken along the AlN $\langle 11\bar{2}0 \rangle$ zone axis. (b) SAD pattern from the circled area in (a). (c) Plan-view TEM image of Sample MOH taken along the AlN $\langle 0001 \rangle$ zone axis. (d) SAD pattern from the circled area in (c). (e) EDS spectra at the two cross-marked points in (c). The strong car- bon peak is due to the residue of the protection film used in the FIB etching process. (f) TEM image at the AlN/γ-AlON interface of Sample MOH. (g) High-resolution TEM image in the rectangle shown in (f). (h) Fourier-filtered image of (g).

petal-shaped multiple domains surrounding the microvoid, respectively. We counted the number of domains for dozens of locations and found that it was either eight or nine. This result suggests that multiple domains are epitaxially oriented on the *r*- and *n*- planes of sapphire, as observed in HVPE-grown AlN on PSS.[42] Figure 4b and d show the corresponding SAD patterns obtained at the circled positions in Fig. 4a and c, exhibiting parallelogram and hexagonal patterns, respectively. From these SAD patterns, we infer that the most likely material composing the domain is spinel-type γ-AlON, as previously reported for an AlN/ sapphire system.[43,44] The simulation using Recipro[45] successfully validated this inference: the lattice spacing for $4\bar{4}0$, $2\bar{2}2$, and 220 in the SAD pattern of Fig. 4b corresponding to 1.57 Å, 2.40 Å, and 2.74 Å is consistent with the simulated values of 1.41 Å, 2.29 Å, and 2.81 Å, respectively, for γ-AlON[45] (see Fig. S6). The discrepancy between the experimental and simulated values could stem from the nonstoichiometric features of AlON with fluctuating lattice constants.[46] In plan-view SAD, the direction along which the satellite spots appear corresponds to the direction from the slope region to the void, which is attributed to the

multiple-electron diffraction for the wedge-shaped γ-AlON sandwiched between the upper AlN and lower sapphire.

As shown in Fig. 4e, EDS analysis also validated the existence of AlON, where a distinct oxygen peak was detected in the petal-shaped domain and not in AlN. Oxygen atoms can be supplied from the sapphire substrate during the FFA and MOVPE growth. Fukuyama et al. reported that γ-AlON is formed via a solid-state reaction between AlN and sapphire during annealing at 1700°C under a N_2 atmosphere, which is the same condition as that used for FFA.[43] Therefore, in the MOH sample, γ-AlON is possibly formed in the slope region during FFA. In addition, fast diffusion through dislocation cores has been reported as a diffusion route for oxygen.[47] Thus, oxygen could sufficiently diffuse from the sapphire substrate to form γ-AlON during MOVPE growth.

The experimentally observed epitaxial relationship of [1$\bar{1}$00]AlN//[110] AlON agrees with the previous studies on the AlN/sapphire system.[43,44] Figure 4f, g, and h show the results of cross-sectional high-resolution TEM observations at the AlN/γ-AlON interface. Figure 4g is the high-resolution image taken at the rectangle area in Fig. 4f. As shown in Fig. 4h, the Fourier filtering in Fig. 4g reveals that the misfit dislocation indicated by the white arrows is periodically introduced at the AlN/γ-AlON interface, which could be the source of threading and basal plane dislocations.

Next, we examined Sample HVC, focusing on the crystalline domain near the microvoid, as shown in Fig. 5. The cross-sectional TEM image shows two separated microvoids

vertically present on the cone pattern of NPSS, while the plan-view TEM image shows a petal-shaped structure with a filled core and six domains. Xiao et al. reported that the upper void was formed owing to the growth mode difference between the cone and flat regions, whereas the lower void was formed via the decomposition of the cone tip at a high growth temperature of 1550°C.[22] For the crystalline domains on the slope regions, we performed SAD analysis and obtained no patterns, suggesting the existence of AlON. Instead, the domains consisted of AlN from the SAD patterns obtained with the zone axes of AlN <11$\bar{2}$1> and <14$\bar{5}$1> shown in Fig. 5b and c for the left and right domains, respectively. The plan-view SAD patterns shown in Fig. 5e and f are identified as those with an AlN <13$\bar{4}$1> zone axis for both diagonal domains. Since the crystal orientations between the cross-sectional and plan-view directions are not correlated (see Table SI), the AlN domains in the slope region are composed of highly misaligned small grains and have a weak epitaxial relationship with the surrounding AlN and sapphire. In addition, cross-sectional TEM images around the slope region reveal that threading dislocations originated from these misaligned AlN domains (Fig. S8). The nonuniformity of domains is a characteristic of Sample HVC in the shape and size fluctuation of the domain–microvoid system compared with those of Sample MOH.

One reason for this difference is the vapor-phase growth condition. Sample HVC employed HVPE growth as the vapor-phase growth method, and it was reported that the
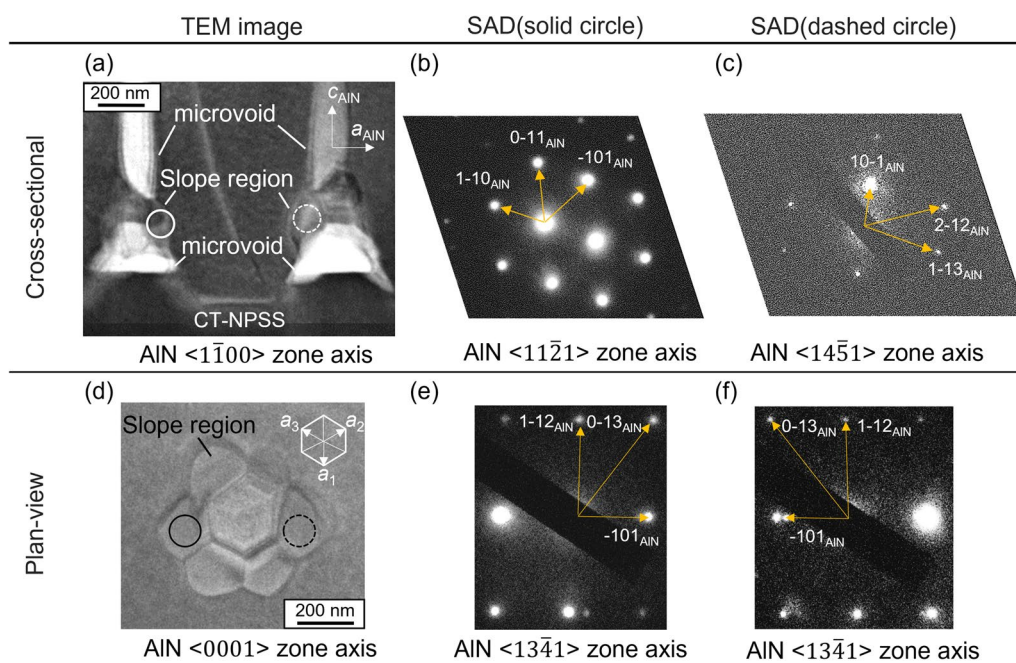
Fig. 5 (a) Cross-sectional TEM image of Sample HVC taken along the AlN{1$\bar{1}$00} zone axis. SAD patterns from the (b) circled area and (c) dotted circled area in (a). (d) Plan-view TEM image of Sample HVC taken along the AlN{0001} zone axis. (e) SAD pattern from the circled area in (d). SAD patterns from the (e) circled area and (f) dashed circled area in (d).

tip of the cone-shaped pattern of NPSS decomposed owing to high-temperature growth at 1550°C.[22] The formation of microvoids in the lower part can be explained by the decomposition of sapphire caused by the reaction with the carrier gas H_2 during AlN growth.[48–50] Table I summarizes the occurrence of sapphire decomposition in the AlN/sapphire templates under various conditions, including the results of previous studies. The occurrence of sapphire decomposition was markedly divided between 1400°C and 1450°C. H_2 was also used during MOVPE growth to fabricate the MOH sample, but the growth temperature was 1300°C. This temperature is probably too low for hydrogen to react with sapphire and cause decomposition. Therefore, the temperature of the vapor-phase growth is a critical parameter, which has a significant impact on controlling the crystal structure in the slope region. Meanwhile, the effect of the NPSS pattern shape on the crystal structure in the slope region is considered relatively small compared with the process temperature, but further investigation is needed to reduce the dislocation density.

Table I Comparison with previous studies on sapphire decomposition in the presence of H_2

Thickness of AlN film (nm)	Temperature (°C)	Occurrence of sapphire decomposition	Author references
180	1300	No occurrence	This study (Sample MOH)
90	1320	No occurrence	Tajima et al.[49]
200	1400	No occurrence	Xiao et al.[22]
50–200	1450	Occurrence	Kumagai et al.[50]
200	1550	Occurrence	This study (Sample HVC)

"Thickness of AlN film" in the table means the thickness of AlN film on sapphire substrates before heat treatment or vapor-phase growth
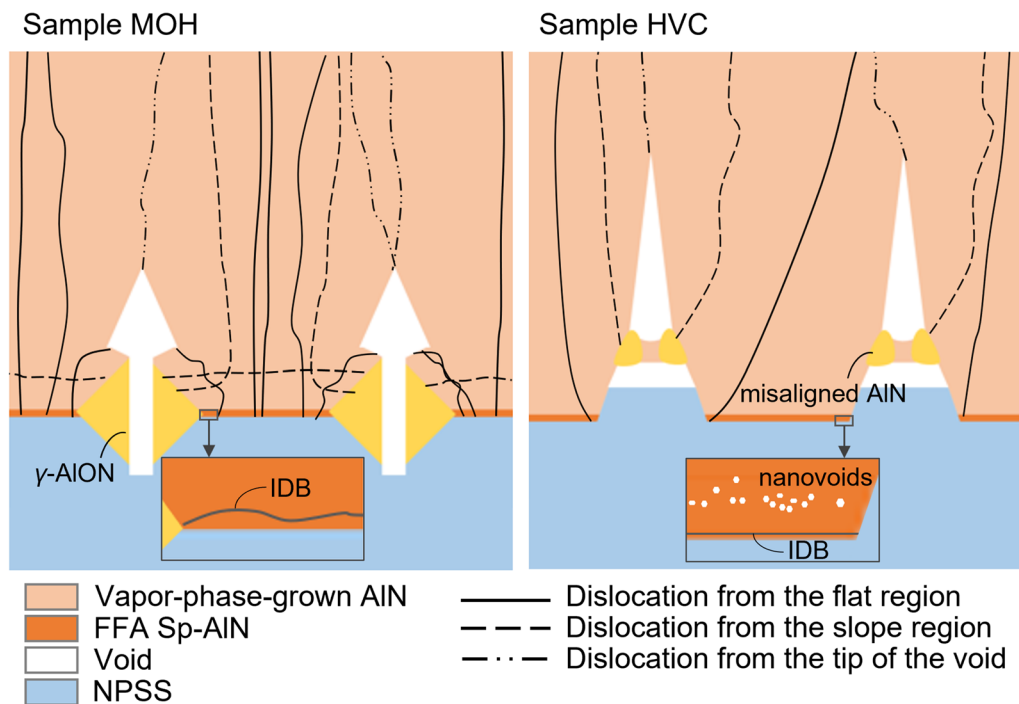
Conclusion

This study analyzed micro- and nanostructures in vapor-phase-grown AlN on FFA Sp-AlN using NPSS. TEM was employed to study the two samples. The observation results for the MOH and HVC samples in the present study are summarized in Table II and Fig. 6. Sample HVC exhibited a lower TDD of 4.7×10^8 cm^{-2} compared to Sample MOH, showing a TDD of 8.3×10^8 cm^{-2} with basal plane dislocations. This difference in crystallinity could originate from the crystal quality of FFA Sp-AlN and the crystalline domains in the slope region. The flat IDB and the presence of nanovoids in the HVC sample are identical to those of the conventional FFA Sp-AlN on the flat sapphire. Conversely, the wavy IDB of Sample MOH has never been observed in conventional FFA Sp-AlN. The crystalline domain observed in the slope region was γ-AlON for the MOH sample and misaligned AlN grains in the HVC sample. We observed that γ-AlON with an epitaxial orientation of [1$\bar{1}$00]AlN//[110] AlON formed misfit dislocations at the interface, which could be converted to dense threading dislocations. Furthermore, the highly misaligned AlN grains had a weak epitaxial orientation with the surrounding c-axis-oriented AlN and sapphire.

Based on the results of this study, it is critical to fabricate FFA Sp-AlN on a flat region and a conventional sapphire substrate. Moreover, the suppression of the formation of singular structures on the slope region is also found to be crucial to further reduce the dislocation density. The optimal sputtering and annealing conditions for FFA Sp-AlN on flat sapphire have been updated,[51,52] which will realize high-quality FFA Sp-AlN on the flat areas of NPSS. The condition of vapor-phase growth can control the crystalline domain formed at the slope region and the shape of the microvoid, which is critical for sufficiently reducing the threading dislocations by avoiding misfit dislocations and enhancing annihilation. Thus, the comprehensive observation of the micro- and nanostructures performed in this study is beneficial for reducing threading dislocations

Table II Comparison table between Sample MOH and Sample HVC

	Sample MOH	Sample HVC
NPSS pattern	Hole type	Cone type
Growth method	MOVPE	HVPE
IDB morphology in the FFA Sp-AlN layer	Waved	Flat
TDD in the flat region	8.3×10^8 cm^{-2}	4.7×10^8 cm^{-2}
Basal plane dislocation	Present	Absent
Crystal structure at the slope region	γ-AlON	Misaligned AlN grains
Epitaxial orientation at the slope region	[1$\bar{1}$00]AlN//[110] AlON	None
Shape uniformity at the slope region	Uniform	Nonuniform

Fig. 6 Schematics of Samples MOH and HVC highlighting the micro- and nanostructures observed in this study.

in vapor-phase-grown AlN and AlGaN on FFA Sp-AlN/ NPSS for high-performance DUV LEDs.

References

1. Y. Taniyasu, M. Kasu, and T. Makimoto, An aluminium nitride light-emitting diode with a wavelength of 210 nanometres. *Nature* (2006). https://doi.org/10.1038/nature04760.
2. H. Hirayama, T. Yatabe, N. Noguchi, T. Ohashi, and N. Kamata, 231–261 nm AlGaN deep-ultraviolet light-emitting diodes fabricated on AlN multilayer buffers grown by ammonia pulse-flow method on sapphire. *Appl. Phys. Lett.* (2007). https://doi.org/10.1063/1.2770662.
3. S. Sumiya, Y. Zhu, J. Zhang, K. Kosaka, M. Miyoshi, T. Shibata, M. Tanaka, and T. Egawa, AlGaN-based deep ultraviolet light-emitting diodes grown on epitaxial AlN/sapphire templates. *Jpn. J. Appl. Phys.* (2008). https://doi.org/10.1143/JJAP.47.43.
4. A. Fujioka, T. Misaki, T. Murayama, Y. Narukawa, and T. Mukai, Improvement in output power of 280-nm deep ultraviolet light-emitting diode by using algan multi quantum wells. *Appl. Phys. Express* (2010). https://doi.org/10.1143/APEX.3.041001.
5. M. Shatalov, W. Sun, A. Lunev, X. Hu, A. Dobrinsky, Y. Bilenko, J. Yang, M. Shur, R. Gaska, C. Moe, G. Garrett, and M. Wraback, AlGaN deep-ultraviolet light-emitting diodes with external quantum efficiency above 10%. *Appl. Phys. Express* (2012). https://doi.org/10.1143/APEX.5.082101.
6. N. Susilo, S. Hagedorn, D. Jaeger, H. Miyake, U. Zeimer, C. Reich, B. Neuschulz, L. Sulmoni, M. Guttmann, F. Mehnke, C. Kuhn, T. Wernicke, M. Weyers, and M. Kneissl, AlGaN-based deep UV LEDs grown on sputtered and high temperature annealed AlN/sapphire. *Appl. Phys. Lett.* (2018). https://doi.org/10.1063/1.5010265.
7. J. Ruschel, J. Glaab, N. Susilo, S. Hagedorn, S. Walde, E. Ziffer, H.K. Cho, N.L. Ploch, T. Wernicke, M. Weyers, S. Einfeldt, and M. Kneissl, Reliability of UVC LEDs fabricated on AlN/sapphire templates with different threading dislocation densities. *Appl. Phys. Lett.* (2020). https://doi.org/10.1063/5.0027769.
8. K. Sato, S. Yasue, Y. Ogino, S. Tanaka, M. Iwaya, T. Takeuchi, S. Kamiyama, and I. Akasaki, Light confinement and high current density in UVB laser diode structure using Al composition-graded p-AlGaN cladding layer. *Appl. Phys. Lett.* (2019). https://doi.org/10.1063/1.5095149.
9. K. Sato, S. Yasue, K. Yamada, S. Tanaka, T. Omori, S. Ishizuka, S. Teramura, Y. Ogino, S. Iwayama, H. Miyake, M. Iwaya, T. Takeuchi, S. Kamiyama, and I. Akasaki, Room-temperature operation of AlGaN ultraviolet-B laser diode at 298 nm on lattice-relaxed $Al_{0.6}Ga_{0.4}N$/AlN/sapphire. *Appl. Phys. Express* (2020). https://doi.org/10.35848/1882-0786/ab7711.
10. H. Amano, R. Collazo, C.D. Santi, S. Einfeldt, M. Funato, J. Glaab, S. Hagedorn, A. Hirano, H. Hirayama, R. Ishii, Y. Kashima, Y. Kawakami, R. Kirste, M. Kneissl, R. Martin, F.

Mehnke, M. Meneghini, A. Ougazzaden, P.J. Parbrook, S. Rajan, P. Reddy, F. Römer, J. Ruschel, B. Sarkar, F. Scholz, L.J. Schowalter, P. Shields, Z. Sitar, L. Sulmoni, T. Wang, T. Wernicke, M. Weyers, B. Witzigmann, Y.-R. Wu, T. Wunderer, and Y. Zhang, The 2020 UV emitter roadmap. *J. Phys. D: Appl. Phys.* (2020). https://doi.org/10.1088/1361-6463/aba64c.

11. M. Kneissl, T.Y. Seong, J. Han, and H. Amano, The emergence and prospects of deep-ultraviolet light-emitting diode technologies. *Nat. Photonics* (2019). https://doi.org/10.1038/s41566-019-0359-9.

12. L. He, W. Zhao, K. Zhang, C. He, H. Wu, X. Liu, X. Luo, S. Li, and Z. Chen, Marked enhancement in the efficiency of deep ultraviolet light-emitting diodes by using a AlxGa1-xN carrier reservoir layer. *Appl. Phys. Exp.* (2019). https://doi.org/10.7567/1882-0786/ab22df.

13. D. Li, K. Jiang, X. Sun, and C. Guo, AlGaN photonics: recent advances in materials and ultraviolet devices. *Adv. Opt. Photonics* (2018). https://doi.org/10.1364/AOP.10.000043.

14. H. Inagaki, A. Saito, H. Sugiyama, T. Okabayashi, and S. Fujimoto, Rapid inactivation of SARS-CoV-2 with deep-UV LED irradiation. *Emerg. Microbes Infect.* (2020). https://doi.org/10.1080/22221751.2020.1796529.

15. H. Kitagawa, T. Nomura, T. Nazmul, K. Omori, N. Shigemoto, T. Sakaguchi, and H. Ohge, Effectiveness of 222-nm ultraviolet light on disinfecting SARS-CoV-2 surface contamination. *Am. J. Infect. Control.* (2021). https://doi.org/10.1016/j.ajic.2020.08.022.

16. H. Kitagawa, T. Nomura, T. Nazmul, R. Kawano, K. Omori, N. Shigemoto, and H. Ohge, Effect of intermittent irradiation and fluence-response of 222 nm ultraviolet light on SARS-CoV-2 contamination. *Photodiagn. Photodyn. Ther.* (2021). https://doi.org/10.1016/j.pdpdt.2021.102184.

17. H. Miyake, C.-H. Lin, K. Tokoro, and K. Hiramatsu, Preparation of high-quality AlN on sapphire by high-temperature face-to-face annealing. *J. Cryst. Growth* (2016). https://doi.org/10.1016/j.jcrysgro.2016.08.028.

18. D. Wang, K. Uesugi, S. Xiao, K. Norimatsu, and H. Miyake, Low dislocation density AlN on sapphire prepared by double sputtering and annealing. *Appl. Phys. Express* (2020). https://doi.org/10.35848/1882-0786/ababec.

19. D. Wang, K. Uesugi, S. Xiao, K. Norimatsu, and H. Miyake, High-quality AlN/sapphire templates prepared by thermal cycle annealing for high-performance ultraviolet light-emitting diodes. *Appl. Phys. Express* (2021). https://doi.org/10.35848/1882-0786/abe522.

20. K. Uesugi, S. Kuboya, K. Shojiki, S. Xiao, T. Nakamura, M. Kubo, and H. Miyake, 263 nm wavelength UV-C LED on face-to-face annealed sputter-deposited AlN with low screw and mixed-type dislocation densities. *Appl. Phys. Express* (2022). https://doi.org/10.35848/1882-0786/ac66c2.

21. Y. Iba, K. Shojiki, K. Uesugi, S. Xiao, and H. Miyake, MOVPE growth of AlN films on nano-patterned sapphire substrates with annealed sputtered AlN. *J. Cryst. Growth* (2020). https://doi.org/10.1016/j.jcrysgro.2019.125397.

22. S. Xiao, N. Jiang, K. Shojiki, K. Uesugi, and H. Miyake, Preparation of high-quality thick AlN layer on nanopatterned sapphire substrates with sputter-deposited annealed AlN film by hydride vapor-phase epitaxy. *Jpn. J. Appl. Phys.* (2019). https://doi.org/10.7567/1347-4065/ab0ad4.

23. C.-H. Chan, C.-H. Hou, S.-Z. Tseng, T.-J. Chen, H.-T. Chien, F.-L. Hsiao, C.-C. Lee, Y.-L. Tsai, and C.-C. Chen, Improved output power of GaN-based light-emitting diodes grown on a nanopatterned sapphire substrate. *Appl. Phys. Lett.* (2009). https://doi.org/10.1063/1.3173817.

24. H. Park, K.-J. Byeon, J.-J. Jang, O. Nam, and H. Lee, Enhancement of photo- and electro-luminescence of GaN-based LED structure grown on a nanometer-scaled patterned sapphire

substrate. *Microelectron. Eng.* (2011). https://doi.org/10.1016/j.mee.2011.07.014.

25. N. Xie, F. Xu, N. Zhang, J. Lang, J. Wang, M. Wang, Y. Sun, B. Liu, W. Ge, Z. Qin, X. Kang, X. Yang, X. Wang, and B. Shen, Period size effect induced crystalline quality improvement of AlN on a nano-patterned sapphire substrate. *Jpn. J. Appl. Phys.* (2019). https://doi.org/10.7567/1347-4065/ab456d.

26. S. Hagedorn, S. Walde, N. Susilo, C. Netzel, N. Tillner, R.-S. Unger, P. Manley, E. Ziffer, T. Wemicke, C. Becker, H.-J. Lugauer, M. Kneissl, and M. Weyers, Improving AlN crystal quality and strain management on nanopatterned sapphire substrates by high-temperature annealing for UVC light-emitting diodes. *Phys. Status Solidi A* (2020). https://doi.org/10.1002/pssa.201900796.

27. L. Zhang, F. Xu, J. Wang, C. He, W. Guo, M. Wang, B. Sheng, L. Lu, Z. Qin, X. Wang, and B. Shen, High-quality AlN epitaxy on nano-patterned sapphire substrates prepared by nano-imprint lithography. *Sci. Rep.* (2016). https://doi.org/10.1038/srep35934(2016).

28. D. Lee, J.W. Lee, J. Jang, I.-S. Shin, L. Jin, J.H. Park, J. Kim, H.-S. Noh, Y.-I. Kim, Y. Park, G.-D. Lee, Y. Park, J. Kim, and E. Yoon, Improved performance of AlGaN-based deep ultraviolet light-emitting diodes with nano-patterned AlN/sapphire substrates. *Appl. Phys. Lett.* (2017). https://doi.org/10.1063/1.4983283.

29. T.-Y. Wang, C.-T. Tasi, K.-Y. Lin, S.-L. Ou, R.-H. Horng, and D.-S. Wuu, Surface evolution and effect of V/III ratio modulation on etch-pit-density improvement of thin AlN templates on nano-patterned sapphire substrates by metalorganic chemical vapor deposition. *Appl. Surf. Sci.* (2018). https://doi.org/10.1016/j.apsusc.2018.06.017.

30. H. Fujikura, T. Konno, T. Kimura, and H. Miyake, AlN nanostructures and flat, void-less AlN templates formed by hydride vapor phase epitaxy on patterned sapphire substrates. *Appl. Phys. Express* (2020). https://doi.org/10.7567/1882-0786/ab65a0.

31. K. Shida, S. Takeuchi, T. Tohei, H. Miyake, K. Hiramatsu, K. Sumitani, Y. Imai, S. Kimura, and A. Sakai, Microstructural analysis in the depth direction of a heteroepitaxial AlN thick film grown on a trench-patterned template by nanobeam x-ray diffraction. *J. Appl. Phys.* (2018). https://doi.org/10.1063/1.5011291.

32. S. Miyake, and R. Uyeda, An exception to Friedel's law in electron diffraction. *Acta Cryst.* (1950). https://doi.org/10.1107/S0365110X5000080X.

33. R. Serneels, M. Snykers, P. Delavignette, R. Gevers, and S. Amelinckx, Friedel's Law in electron diffraction. *Phys. Stat. Sol.* (1973). https://doi.org/10.1002/pssb.2220580127.

34. L.T. Romano, J.E. Northrup, and M.A. Okeefe, Inversion domains in GaN grown on sapphire. *Appl. Phys. Lett.* (1996). https://doi.org/10.1063/1.117648.

35. N. Stolyarchuk, T. Markurt, A. Courville, K. March, J. Zúñiga-Pérez, P. Vennéguès, and M. Albrecht, Intentional polarity conversion of AlN epitaxial layers by oxygen. *Sci. Rep.* (2018). https://doi.org/10.1038/s41598-018-32489-w.

36. S. Xiao, R. Suzuki, H. Miyake, S. Harada, and T. Ujihara, Improvement mechanism of sputtered AlN films by high-temperature annealing. *J. Cryst. Growth.* (2018). https://doi.org/10.1016/j.jcrysgro.2018.09.002.

37. K. Shojiki, K. Uesugi, S. Kuboya, T. Inamori, S. Kawabata, and H. Miyake, High-quality AlN template prepared by face-to-face annealing of sputtered AlN on sapphire. *Phys. Status Solidi B* (2021). https://doi.org/10.1002/pssb.202000352.

38. T. Akiyama, M. Uchino, K. Nakamura, T. Ito, S. Xiao, and H. Miyake, Structural analysis of polarity inversion boundary in sputtered AlN films annealed under high temperatures. *Jpn. J. Appl. Phys.* (2019). https://doi.org/10.7567/1347-4065/ab0d01.

39. S. Mohn, N. Stolyarchuk, T. Markurt, R. Kirste, M.P. Hoffmann, R. Collazo, A. Courville, R. Di Felice, Z. Sitar, P. Vennéguès, and

M. Albrecht, Polarity control in group-III nitrides beyond pragmatism. *Phys. Rev. Appl.* (2016). https://doi.org/10.1103/PhysRevApplied.5.054004.

40. Z. Zhang, Y. Hayashi, T. Tohei, A. Sakai, V. Protasenko, J. Singhal, H. Miyake, H.G. Xing, D. Jena, and Y. Cho, Molecular beam homoepitaxy of N-polar AlN: enabling role of aluminum-assisted surface cleaning. *Sci. Adv.* (2022). https://doi.org/10.1126/sciadv.abo6408.

41. Y. Tokumoto, N. Shibata, T. Mizoguchi, M. Sugiyama, Y. Shimogaki, J.-S. Yang, T. Yamamoto, and Y. Ikuhara, High-resolution transmission electron microscopy (HRTEM) observation of dislocation structures in AlN thin films. *J. Mater. Res.* (2008). https://doi.org/10.1557/JMR.2008.0265.

42. S. Xiao, K. Shojiki, and H. Miyake, Thick AlN layers grown on micro-scale patterned sapphire substrates with sputter-deposited annealed AlN films by hydride vapor-phase epitaxy. *J. Cryst. Growth* (2021). https://doi.org/10.1016/j.jcrysgro.2021.126163.

43. H. Fukuyama, H. Miyake, G. Nishio, S. Suzuki, and K. Hiramatsu, Impact of high-temperature annealing of AlN layer on sapphire and its thermodynamic principle. *Jpn. J. Appl. Phys.* (2016). https://doi.org/10.7567/JJAP.55.05FL02.

44. S. Hagedorn, S. Walde, A. Mogilatenko, M. Weyers, L. Cancecllara, M. Albrecht, and D. Jaeger, Stabilization of sputtered AlN/sapphire templates during high temperature annealing. *J. Cryst. Growth* (2019). https://doi.org/10.1016/j.jcrysgro.2019.02.024.

45. Y. Seto and M. Ohtsuka, ReciPro: free and open-source multipurpose crystallographic software integrating a crystal model database and viewer, diffraction and microscopy simulators, and diffraction data analysis tools. *J. Appl. Cryst.* (2022). https://doi.org/10.1107/S1600576722000139.

46. N.D. Corbin, Aluminum oxynitride spinel: a review. *J. Euro. Ceram. Soc.* (1989). https://doi.org/10.1016/0955-2219(89)90030-7.

47. L. Cancellara, T. Markurt, T. Schulz, M. Albrecht, S. Hagedorn, S. Walde, M. Weyers, S. Washiyama, R. Collazo, and Z. Sitar, Role of oxygen diffusion in the dislocation reduction of epitaxial AlN on sapphire during high-temperature annealing. *J. Appl. Phys.* (2021). https://doi.org/10.1063/5.0065935.

48. K. Akiyama, T. Araki, H. Murakami, Y. Kumagai, and A. Koukitu, In situ gravimetric monitoring of decomposition rate on the surface of (0001) c-plane sapphire for the high temperature growth of AlN. *Phys. Stat. Sol.* (2007). https://doi.org/10.1002/pssc.200674816.

49. J. Tajima, Y. Kubota, R. Togashi, H. Murakami, Y. Kumagai, and A. Koukitu, Growth of thin protective AlN layers on sapphire substrates at 1065 ºC for hydride vapor phase epitaxy of AlN above 1300 ºC. *Phys. Stat. Sol.* (2008). https://doi.org/10.1002/pssc.200778433.

50. Y. Kumagai, Y. Enatsu, M. Ishizuki, Y. Kubota, J. Tajima, T. Nagashima, H. Murakami, K. Takada, and A. Koukitu, Investigation of void formation beneath thin AlN layers by decomposition of sapphire substrates for self-separation of thick AlN layers grown by HVPE. *J. Cryst. Growth* (2010). https://doi.org/10.1016/j.jcrysgro.2010.04.008.

51. K. Uesugi, Y. Hayashi, K. Shojiki, and H. Miyake, Reduction of threading dislocation density and suppression of cracking in sputter-deposited AlN templates annealed at high temperatures. *Appl. Phys. Express* (2019). https://doi.org/10.7567/1882-0786/ab1ab8.

52. K. Uesugi, K. Shojiki, S. Xiao, S. Kuboya, and H. Miyake, Effect of the sputtering deposition conditions on the crystallinity of high-temperature annealed AlN films. *Coatings* (2021). https://doi.org/10.3390/coatings11080956.